

Modeling of excimer laser ablation of silicon carbideChen Lu, Meng-meng Gao, Ting-ting Hu, and Zhi-zhan Chen **Department of Physics, Shanghai Normal University, 100 Guilin Road, Shanghai 200234, China*

(Received 28 July 2021; revised 25 August 2021; accepted 30 August 2021; published 14 September 2021)

The physical model of nanosecond laser ablation of semi-insulating 4H-SiC irradiated by KrF excimer laser with a wavelength of 248 nm was studied. The etching depth was tested by a stylus surface profiler. The morphology of the ablation pit and the thickness of the damaged layer were observed through scanning electron microscope. The phases at the laser irradiated surface were analyzed by Raman spectroscopy. *In situ* x-ray photoelectron spectroscopy was used to obtain component distribution of the damaged layer and a reasonable thermophysical model was constructed. The temperature distribution of the substrate after the laser irradiation was calculated according to this model. It was found that the etching depth had a linear relationship with the number of laser pulses and the thickness of the uniform damaged layer was independent of pulse number (>10). The thickness of the ablated layer and the newly generated damaged layer are equivalent for each laser irradiation. The established laser ablation model deepens the understanding of physical process and mechanism of nanosecond laser etching of SiC and provides a theoretical guidance for laser processing of SiC.

DOI: [10.1103/PhysRevB.104.115304](https://doi.org/10.1103/PhysRevB.104.115304)**I. INTRODUCTION**

Silicon carbide (SiC) is a wide-gap semiconductor with mature growth technology [1]. Currently, high-quality 6-inch bulk and epitaxial single crystals of SiC are commercially available. SiC has attractive properties such as wide band gap, high breakdown electric field, high thermal conductivity, chemical inertness, and strong mechanical hardness [2]. Based on its excellent performance, SiC has become the most promising wide band-gap semiconductor for high-temperature, high-frequency, and high-power applications [3]. Unfortunately, some of these characteristics are also obstacles to the manufacture of microelectronics and Micro-Electro-Mechanical System (MEMS) SiC-based devices. Therefore, laser processing has attracted great research interest and has been applied in some areas such as annealing, hole drilling, *in situ* doping, and micromachining [4–9]. Micromachining is a critical step in SiC device manufacturing. Laser etching technology can obtain high-quality microstructures in a shorter time due to its high controllability of parameters (such as wavelength, repetition frequency, laser fluence, pulse width, and so on) and high etching rate. Since the bond energy of the Si-C bond is 375 kJ/mol [10], the laser wavelength corresponding to this energy is 320 nm [11]. In addition, the band gap of 4H-SiC is 3.23 eV, and the corresponding wavelength is 385 nm, which means the absorption of light in the UV band by SiC is dominated by intrinsic absorption. In this case, the heating mechanism is to excite excess carriers and transfer energy to the lattice through the interaction between electrons and phonons [12]. Furthermore, it has been reported in experiment that SiC has a nearly linear correlation between the number of pulses and etching depth [13], independent of

laser fluence, which makes the UV lasers excellent choices for micromachining of SiC-based MEMS devices.

The mechanism of laser ablation of SiC by excimer lasers has been investigated experimentally and theoretically by researchers in the past decades. Dutto *et al.* numerically simulated the process of excimer lasers irradiating SiC based on the heat flow equation and the result was in good agreement with the experiment. Their model can predict the thermal behavior of SiC well when the temperature is below the melting point of SiC [14]. However, the condition when the temperature is higher than the melting point of SiC is not mentioned. Retano measured the ablation rate of SiC crystal targets induced by XeCl excimer laser pulses as function of the laser fluence over a wide range and calculated the evaporation rate [15]. Yet, in their work, the inconsistency of the heating process due to graphite and silicon generated by the decomposition of SiC at high temperatures was not considered. Mohammed *et al.* reported the decomposition of SiC after being irradiated by ArF excimer laser and the relationship between the etching rate and laser fluence. Through the finite-element simulation, the corresponding temperature rise of SiC under different energy densities was given [16]. In their work, no attention was paid to the effect of the substance distribution of the damaged layer of SiC on the thermal properties of the substrate after laser irradiation.

Although there have been many reports on laser ablation of SiC, the mechanism of laser ablation of SiC during the etching process has not been elucidated. In this contribution, the laser etching SiC model was established through *in situ* x-ray photoelectron spectroscopy, and the thermal physical mechanism was explained by numerical calculation. Compared to the existing reports, more attention was paid to the damaged layer near the surface of SiC after laser irradiation and its substance distribution with depth. More significantly, our calculation takes the temperature dependence of the

*zzchen@shnu.edu.cn

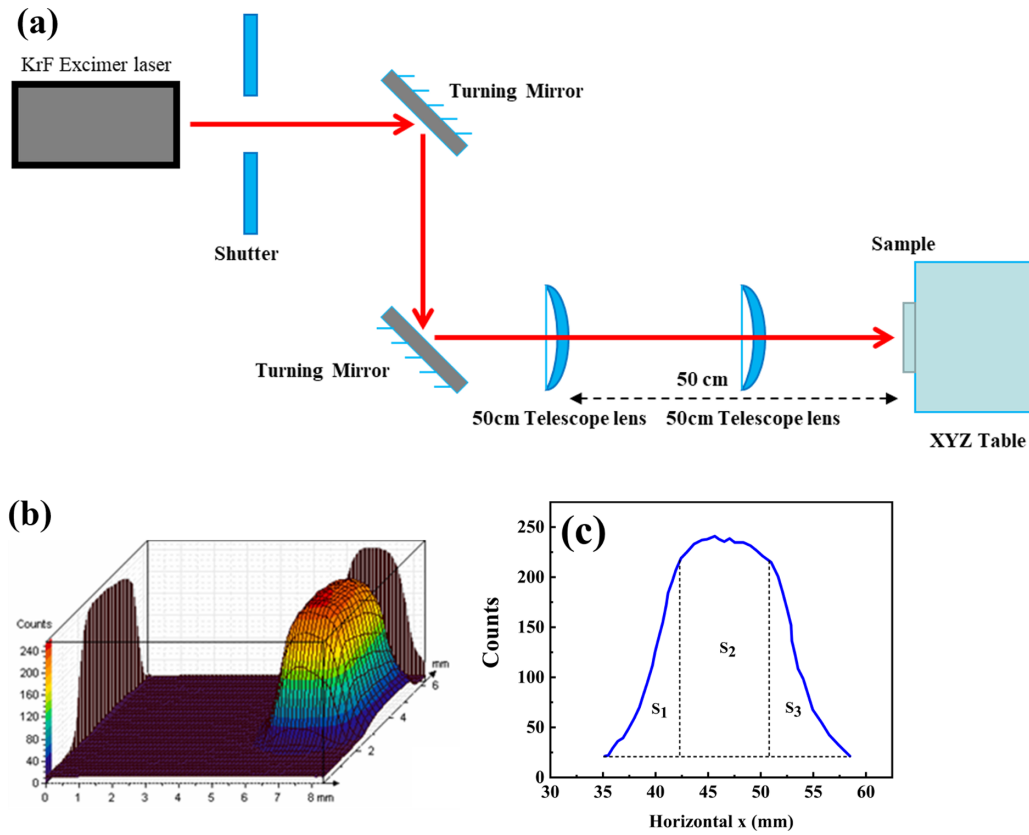


FIG. 1. (a) Light path applied in this experiment. (b) Spatial distribution of the laser spot intensity. (c) Light-intensity distribution of the short axis of the spot.

thermal parameters of SiC, the decomposition of SiC at high temperatures with the evaporation of the substance, and the change of the substance phase into account, which makes our calculation are in good agreement with the experimental phenomena.

II. EXPERIMENT

The 350- μm -thick semi-insulating 4H-SiC wafer was used. The wafer was cleaned by the Radio Corporation of America method. The laser irradiation was performed by the ultraviolet pulse KrF excimer laser (COMPEXPRO201, Germany). The wavelength is 248 nm, the maximum repetition rate is 10 Hz, and the pulse width is 25 ns. The light path applied in the experiment is demonstrated in Fig. 1(a). The laser was irradiated onto the substrate through two mirrors and two convex lenses with a focal length of 50 cm. The energy output pulse waveform is rectangular. The shape of the laser spot impinging onto the substrate is rectangular with a size of about 0.9 mm \times 2.2 mm. To ensure that a more accurate energy of the laser reaches the substrate, the sensor of the laser energy meter (Labmax-top, Coherent, USA) with an inaccuracy of $\pm 1\%$ was placed at the position of the substrate, where the measured value was 164 mJ; however, when the sensor was placed at the output of the laser, the measured energy was 400 mJ, which was consistent with the setting of the laser control panel. Due to the reflection in the mirror and the lens transmission, the laser loses about 59% of the energy. The laser fluence is calculated as the laser energy (164 mJ)

measured using a laser energy meter divided by the ablation pit area (0.9 mm \times 2.2 mm) measured by optical microscope. However, it is worth noting that the sensor receives the energy of the entire spot area (i.e., the actual laser spot is larger than the ablation pit area). As shown in Fig. 1(b), the spatial distribution of the laser in the short axis is approximately Gaussian and is flat topped in the long axis. Figure 1(c) shows light-intensity distribution of the short axis of the spot. In the short-axis direction, the light intensity drops sharply for $x < x_l$ and $x > x_r$. The inhomogeneity of the laser energy in the edge area can lead to large errors in the measurement of the ablation depth and the thickness of the damaged layer, because the material evaporated from the solid target under laser irradiation migrates to the edge region under the effect of the temperature gradient. For the accuracy of the test, we only consider the region of relatively uniform light-intensity distribution, i.e., $x_l < x < x_r$, in our experiments and calculations. The ratio of the laser energy in this region to the overall laser energy should be $S_2/(S_1 + S_2 + S_3)$, which is about 0.543. Thus, the laser fluence is calculated to be about $4.5 \pm 0.1 \text{ J/cm}^2$. Eleven samples with (000 $\bar{1}$) surface were irradiated 1, 2, 3, 4, 5, 10, 20, 30, 50, 70, and 1000 times at a laser fluence of $4.5 \pm 0.1 \text{ J/cm}^2$ and the pulse repetition rate was 1 Hz. The etching depth was obtained by scanning inside the ablation pit parallel to the short axis repeatedly using a stylus surface profiler (DEKTA-K-XT, Germany) and intercepted the average value of the height difference between the central position at the bottom of the ablation pit and the initial horizontal position.

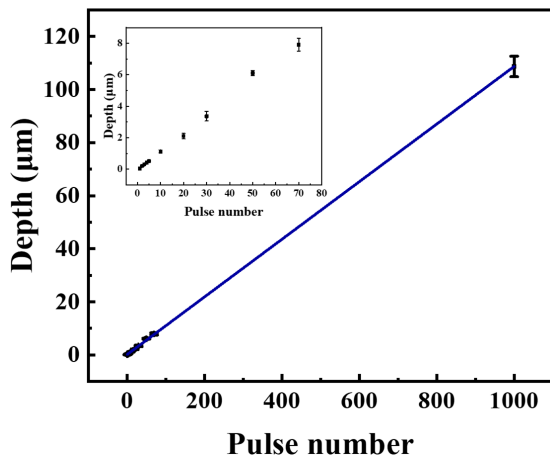


FIG. 2. Relationship between the etching depth of semi-insulating 4H-SiC ablated by KrF excimer laser and N .

After laser irradiation, the scanning electron microscope (SEM, Hitachi S-4700) was used to observe the surface morphology. The elemental analysis was performed using *in situ* x-ray photoelectric spectroscopy (XPS, PHI 5000C, PerkinElmer). A Raman spectrometer (Lab RAM HR800, France) with 355-nm excitation lines was used to investigate the phase evolution with a 100× magnification microscope objective.

III. RESULTS AND DISCUSSION

The dependence of etching depth (the total thickness of the ablated layer in the central area of the ablation pit) at the irradiation fluence of $4.5 \pm 0.1 \text{ J/cm}^2$ with the numbers of pulse (N) is shown in Fig. 2. When N is 1, the etching depth is $42.5 \pm 3.6 \text{ nm}$, as shown in the inset of Fig. 2. As N increases, the etching depth versus N almost follows a linear relationship, and etching rate is approximately equal to 108 nm per pulse. Why does the etching depth have a linear relationship with the number of laser pulses, except for the first pulse of irradiation?

To answer the above question, first, the surface and cross-section SEM morphologies of the central area of the ablated spot after 70 shots were observed, as shown in Fig. 3. Extremely regular grooves with spacing of $7.6 \mu\text{m}$ were identified as shown in Fig. 3(a). The same phenomenon was also reported by Birnbaum [17]. According to our observations, these grooves might be formed by the fusion of fine ripples with a period of approximately the wavelength of the incident light formed at the initial stage of irradiation, which were possibly formed by the interference between the incident laser and surface plasmon polaritons [18–22]. The fusion of fine ripples is probably led by hydrothermal waves perpendicular to the thermal gradient, which are dominated by convection generated by Marangoni shear. In this process, recoil pressure, surface tension differences, and temperature gradients play crucial roles [23]. Figure 3(b) is the enlarged image of the circled part in Fig. 3(a). The ablation surface is covered with a layer of spherical nanoparticles with a diameter of 30–50 nm. Figure 3(c) is the cross-section morphology of the ablated spot. The cross section of the stripes formed on

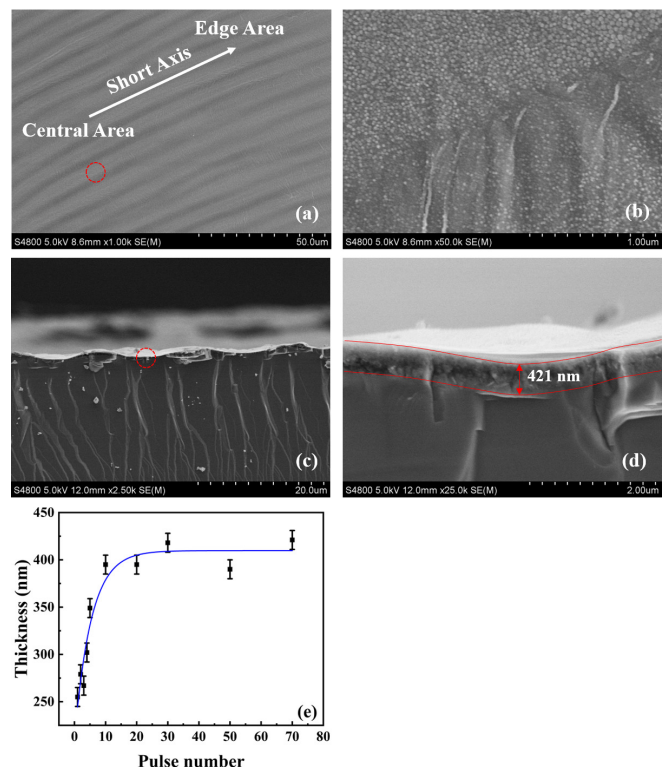


FIG. 3. Scanning electron morphologies of the surface (a) and the cross section (c) of the ablated spot after 70 pulses shot. (b) and (d) are the enlarged image of the circled part in (a) and (c), respectively. (e) Relationship between the thickness of damaged layer and the numbers of pulse.

the surface can be observed to be wavy. From its enlarged image [Fig. 3(d)], it is found that a layer of molten material with obvious ablation traces and distinct from the substrate was formed on the surface, whose thickness is about $421 \pm 10 \text{ nm}$. Hereafter, this layer is called damaged layer, and the thickness of damaged layer is abbreviated as TDL. TDL is characterized by measuring the distance between the interface of the damaged layer and the substrate and the surface of the ablation crater [i.e., the distance between the two red lines in Fig. 3(d)]. The TDL versus N is shown in Fig. 3(e). When N is less than 10, TDL is linearly increased. However, TDL is essentially independent of N when N is more than 10, and it approaches a saturation value of $400 \sim 420 \text{ nm}$.

Raman spectra of samples can be used to investigate the composition of the damaged layer. Here, the substrate spectrum is obtained at the nonirradiated area, far from the irradiated area, and can be considered as a reference. As shown in Fig. 4, the sharp peaks at $769, 790, \text{ and } 969 \text{ cm}^{-1}$ originate from acoustic/optical phonons produced in nonirradiated 4H-SiC crystal. After laser irradiation, Raman peaks of 4H-SiC crystal disappear while the 519-cm^{-1} peak appears which can be attributed to amorphous silicon (a-Si). On the other hand, the bands of amorphous graphite also appear around 1400 cm^{-1} (D band) and 1593 cm^{-1} (G band). The results of the Raman measurement confirm that the sample has undergone phase changes near the surface even when the first pulse arrives. The substance formed by the subsequent

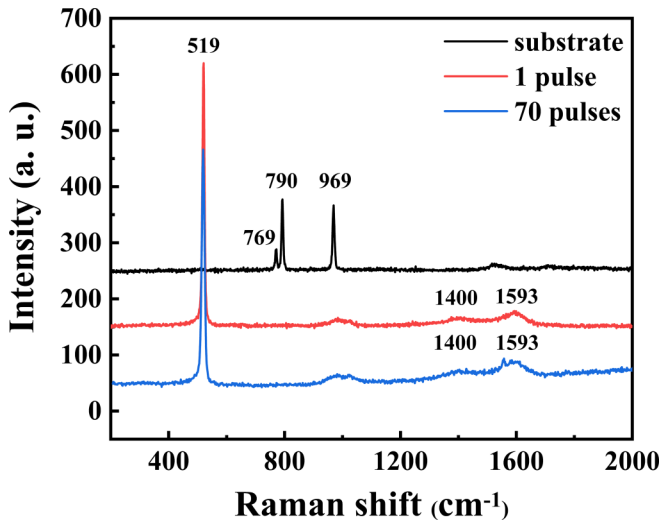


FIG. 4. 355-nm Raman spectra of the substrate and the substrate irradiated once and 70 times by laser.

repeated pulses is almost the same as the substance of the damaged layer at the end of the first pulse.

In situ XPS measurements are also performed on the damaged layer analysis of laser-irradiated samples at different depths to get more information about compound phases and their contents. The C1s and Si2p core-level XPS spectra of laser-irradiated samples for 1, 10, and 70 times through XPS peak differentiation imitating analysis are shown in Figs. 5(a)–5(c), respectively. Generally speaking, it can be seen from the C1s spectrum that C–Si bond (~283.4 eV) [24] and C–C bonds (284.5, ~284.8, and ~285.5 eV) are observed for three samples. Among them, the C–Si bond can be classified as SiC that is not decomposed, while the first C–C bond located at 284.5 eV can be assigned to graphite generated by SiC decomposition during irradiation. Furthermore, the second C–C bond located at 284.8 eV was attributed to the external contamination (hereafter designated as CTM for brevity). However, an unidentified C–C bond located at ~285.5 eV (marked as UG), which is clearly distinct from graphite, is first reported. Because the instantaneous temperature of SiC crystal can reach more than 3100 K (discussed later) after laser irradiation, and the thermal pressure inside the crystal reaches as high as 10^3 – 10^4 bar, such conditions may promote the transformation of graphite to diamond [25]. This is the reason why the binding energy (BE) of C–C bond is redshift. In the Si2p spectrum, Si–Si bond (~99.5 eV), Si–C bond (~100.2 eV) [24], and Si–O bond (~102.4 eV) can be identified, corresponding to Si, SiC, and SiO_x, respectively. The O1s spectrum is not displayed here because the oxygen in the samples is only from silicon oxide (SiO_x) as well as external contamination.

The changes of XPS spectra at different depths under different irradiation times are carefully analyzed. For the sample irradiated once, no C–Si bond is detected on the surface; instead, the Si–Si bonds at 99.48 eV and Si–O bond at 102.00 eV appear as shown in Figs. 5(a1) and 5(a7), indicating that the SiC surface has been modified. Both the thermal decomposition of SiC and subsequent recrystallization of Si

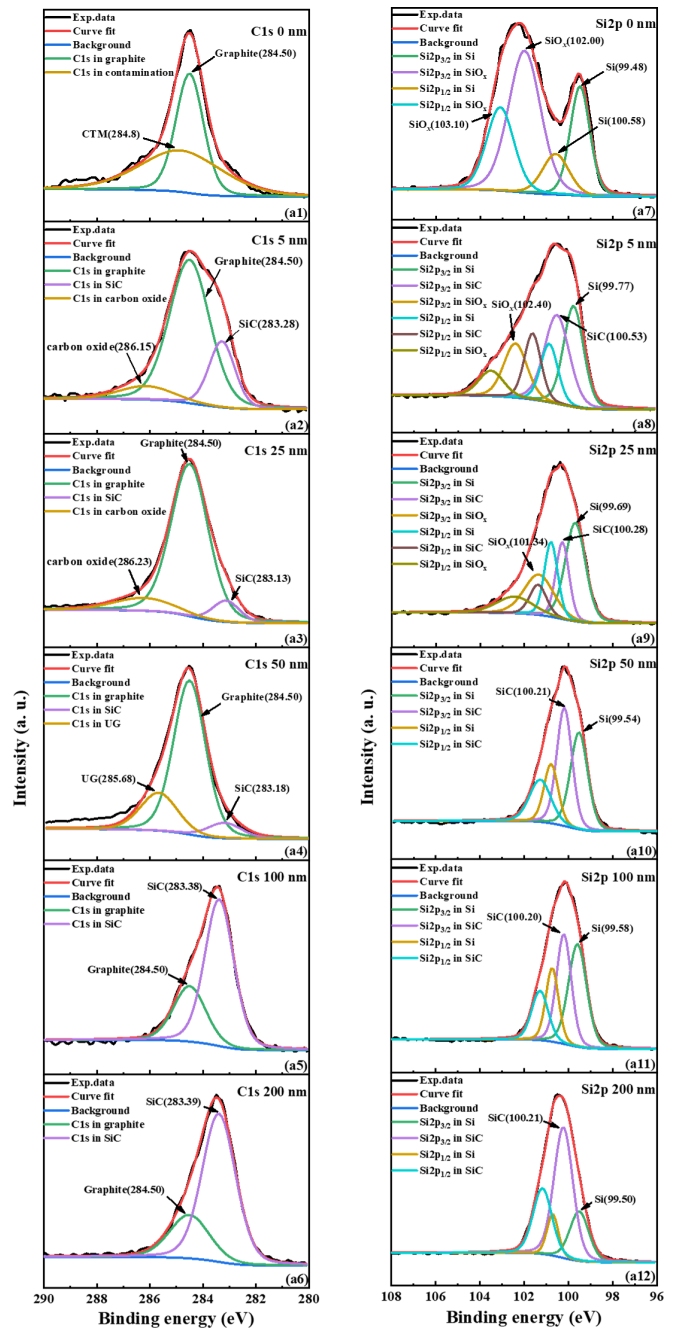


FIG. 5. (a1)–(a12), (b1)–(b12), and (c1)–(c12) are the C1s, Si2p core-level spectra. (d1)–(d3) are the molar ratio (with an inaccuracy of $\pm 2.5\%$), and (e1)–(e3) are simplified schematics of component distribution in different depth of the samples irradiated 1, 10, and 70 times, respectively.

vapor result in the formation of Si phases, while part of them has been oxidized to form SiO_x in the air atmosphere. The result is consistent with Raman spectra. Unlike the case of the surface, the C–Si bonds at about 283 eV in C1s spectra [Figs. 5(a2)–5(a6)] and at about 100 eV in Si2p spectra [Figs. 5(a8)–5(a12)] start to appear from 5 nm onwards, suggesting the existence of SiC phase. It is worth noting that the BE of C–Si bond in Si2p spectra exhibits the blueshift phenomenon (0.3 eV) as the etching depth increases, i.e., the BE

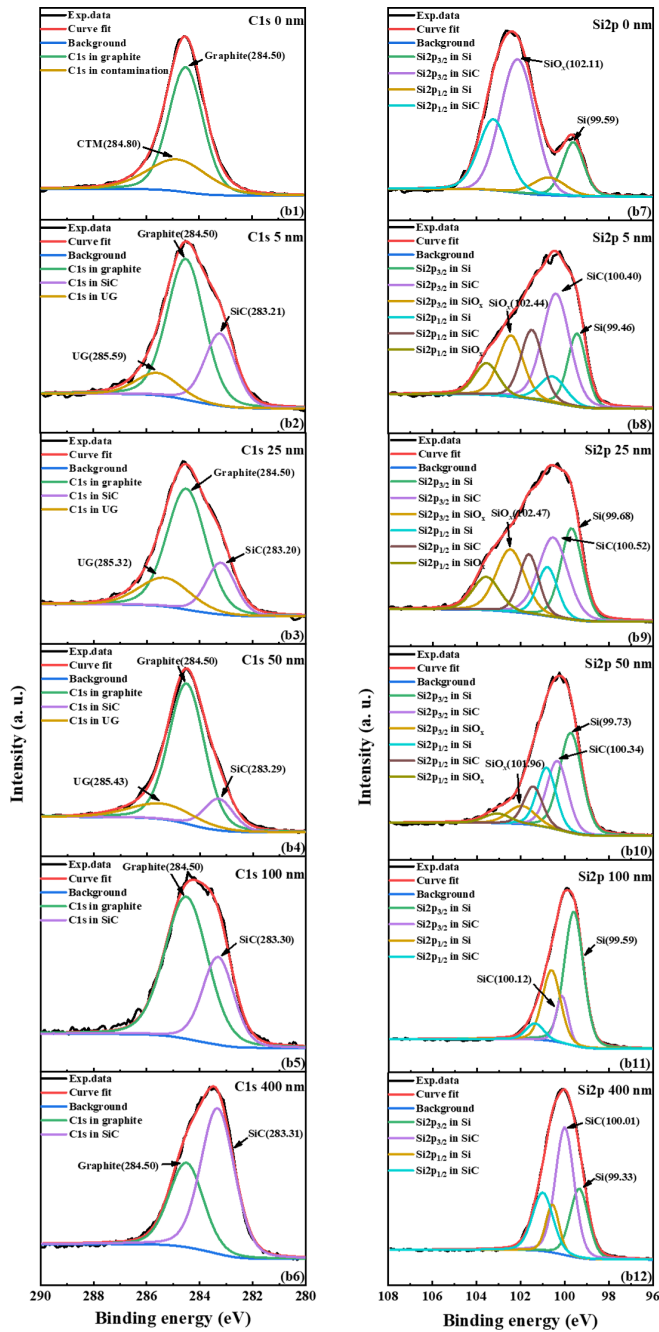


FIG. 5. (Continued.)

is 100.53, 100.28, and 100.21 eV at the depths of 5, 25, and 200 nm, respectively. The BE of 100.53 eV is consistent with that of 3C-SiC, which suggests that either phase transformation from 4H-SiC to 3C-SiC or recrystallization from Si vapor and graphite to form 3C-SiC occurs at the near surface after laser irradiation. The same phenomenon has been reported in our previous work [26]. The molar ratios of silicon, graphite, and SiC in different depths can be calculated by their peak areas. Since SiO_x is formed by the oxidation of monomeric Si, Si in SiO_x is counted as monomeric Si in the calculation. The normalized result of the sample irradiated one time is shown in Fig. 5(d1). The molar ratios of them are relatively close to each other in the depths of 0–25 nm. The ratio of graphite in

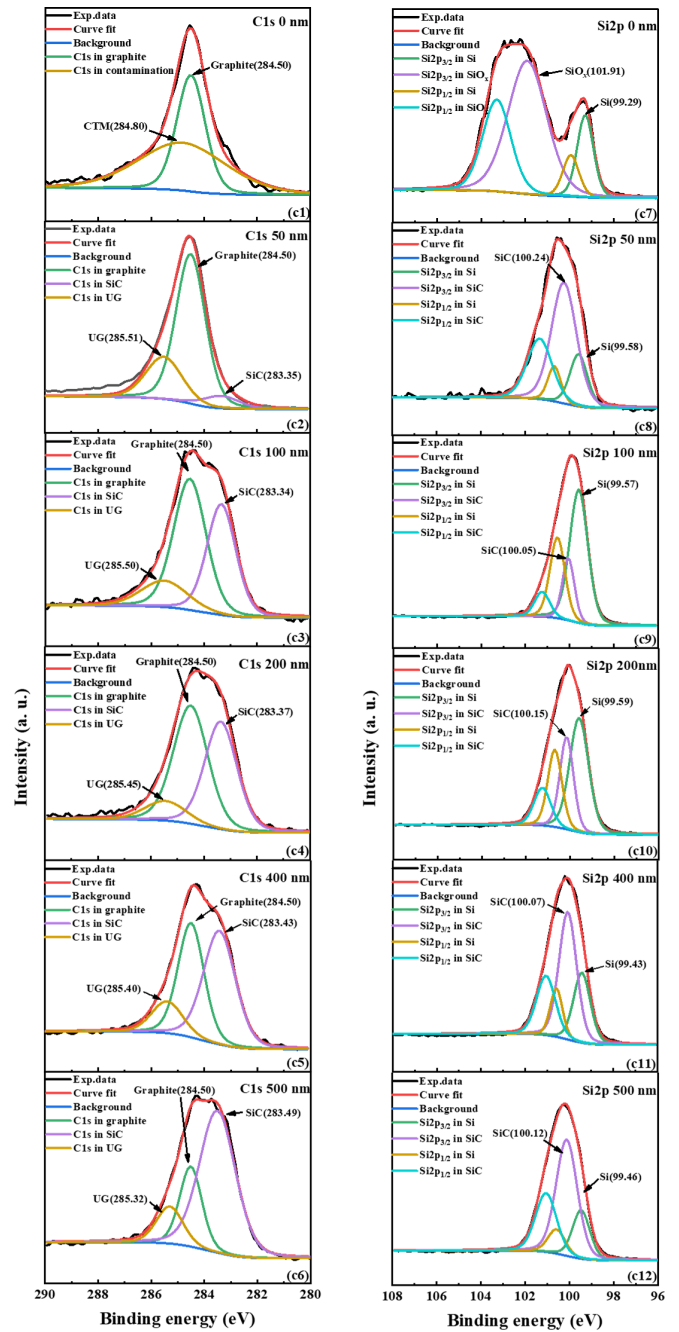


FIG. 5. (Continued.)

the depth of 25–50 nm reaches more than 60%, even up to 76.9% at 50 nm. In the depths above 50 nm, the ratio of SiC rises rapidly and becomes the most predominant component at 100 nm (55.8%), while the ratio of graphite decreases rapidly, and the ratio of Si rises slightly. Therefore, the depth of 50–100 nm can be regarded as a transition domain. The result at 150 nm is not presented in the figure since the bonds that exist in the depth from 100 to 200 nm and their trends are consistent. Based on the above discussion, the component distribution near the surface of SiC after one exposure to laser irradiation can be simplified in Fig. 5(e1).

As for the sample irradiated ten times, the component composition of the surface is the same as that of the sample

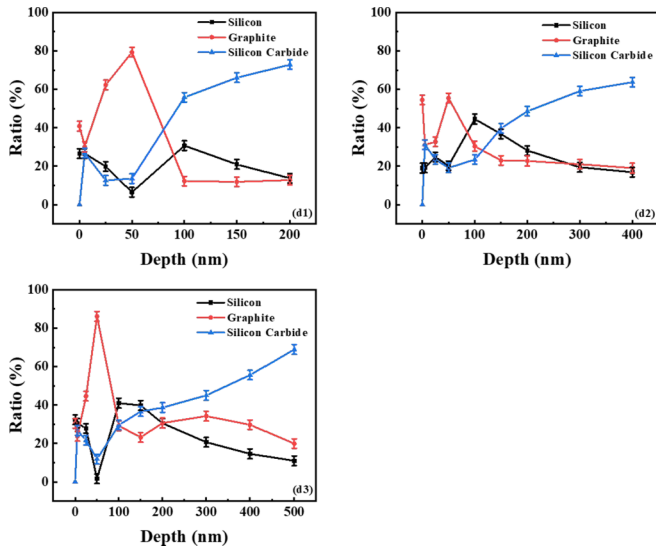


FIG. 5. (Continued.)

irradiated one time, and no C–Si bond is detected as well [Figs. 5(b1) and 5(b7)]. Compared with the case of one pulse irradiation, the content of C–Si bond continues to decrease in the depth of 25–50 nm [Figs. 5(b3), 5(b9) and 5(b4), 5(b11)], which indicates that the damage of SiC is more severe after ten pulses irradiation. It is noteworthy that after ten irradiations, the ratio of SiC is significantly decreased in the 100–200-nm depth compared to the sample irradiated one time as shown in Fig. 5(d2). It indicates that a larger amount of SiC is destroyed and decomposed to form Si and graphite during repeated irradiation. This is the reason why the molar ratio of Si to graphite in this region is greater for the sample irradiated ten times than that of the sample irradiated one time. At a depth of 200 nm, the SiC content reaches 48.58%, substantially ahead of Si and graphite. Thus, the component distribution in the damaged layer after ten irradiations is simplified in Fig. 5(e2). The situation was similar for 70 pulses to 10 pulses, except that the SiC content decreased slightly [Fig. 5(d3)] at the same depth due to more decomposition of SiC as the numbers of pulse increased, but the overall trend remained unchanged. The components at different depths are simplified in Fig. 5(e3). Summing up Fig. 5, we can find that no matter how many times of irradiation, the composition of the damaged layer can be divided into three sublayers. The first sublayer, from the surface to 25 nm, is a mixture of graphite (with the most content), Si and SiC, and the second sublayer, from 25

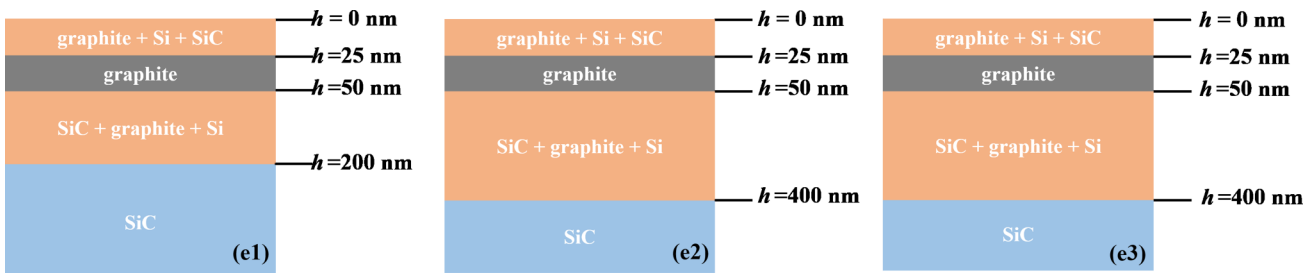


FIG. 5. (Continued.)

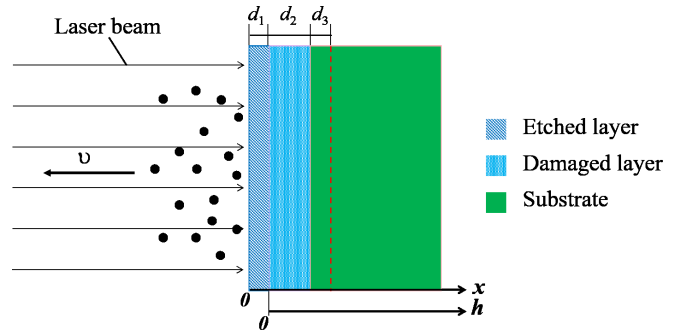


FIG. 6. Simplified schematic diagram of the ablation process of SiC. d_1 , d_2 , and d_3 represent the thickness of the etched layer, the remaining damaged layer, and the newly formed damaged layer after each laser irradiation, respectively.

to 50 nm, is mainly composed of graphite. The thickness of the third sublayer, which also consists of SiC, silicon, and graphite, increases with the number of irradiations until ten irradiations and stabilizes at 350 nm after ten irradiations. It should be emphasized that the component distribution barely changes with the increase in the number of pulses except the minor variation of molar ratios.

According to the experimental results, the temperature distribution is obtained by numerical calculation. Before calculating, it is necessary to make clear the meaning of two “surfaces,” *i.e.*, experimental surface and computational surface. The former refers to the objectively observed surface after laser irradiation, while the latter to the surface of the sample before laser irradiation. The reason for the difference is that the substrate may be ablated by laser irradiation, as shown in Fig. 6. Two different coordinate systems will be used in the following discussion, and the relationship between them is $x = h + d_1$, where x is the coordinate system in the computational part, h is in the experimental part, and d_1 is the thickness of the etched layer.

For the first pulse irradiation, the process can be divided into two stages, where stage 1 refers to the substrate temperature less than the melting point of SiC (3100 K) while stage 2 to that more than 3100 K. As the size of the laser spot is much larger than the penetration depth of the laser on SiC, a one-dimensional situation will be a good approximation. Assuming the heat exchange in the SiC body mainly relies on heat conduction, the following heat conduction-coupling diffusion equations can describe the temperature (T) and car-

rier concentration (n) changes with time t and depth z [27] in stage 1:

$$\frac{\partial n}{\partial t} = \frac{\partial}{\partial z} \left\{ D \frac{\partial n}{\partial z} + D \frac{n}{2T} \left[1 + \frac{1}{k_B} \left(\frac{\partial E_g}{\partial T} \right) \right] \frac{\partial T}{\partial z} \right\} + \frac{I(t)(1-R)\alpha e^{-\alpha z}}{\hbar\omega} - \gamma n^3, \quad (1)$$

$$\frac{\partial T}{\partial t} = \frac{\partial}{\partial z} \left(D_L \frac{\partial T}{\partial z} \right) + \frac{\eta I(t)(1-R)\alpha e^{-\alpha z}}{C} \frac{\hbar\omega - E_g - 3k_B T}{\hbar\omega} + \frac{\gamma n^3}{C} (E_g + 3k_B T), \quad (2)$$

where Eq. (1) gives the change of excess carrier concentration. The first term on the right is the current density of electron-hole pairs, the second one is the absorption of photons by the substrate, and the third one is Auger recombination; Eq. (2) gives the temperature field distribution of the substrate. The first term on the right refers to the thermal diffusion, and the second and third ones refer to the heat sources from intrinsic absorption and Auger recombination, respectively. The physical meaning of each parameter is as follows: D is the ambipolar diffusion coefficient, E_g is the band gap (here the influence of temperature on E_g is considered), $I(t)$ is the laser intensity, R is the reflectivity, α is the absorption coefficient, and γ is the Auger recombination coefficient, T is the lattice temperature, D_L is the thermal diffusion coefficient, C is the specific heat, η is the quantum efficiency, and k_B is the Boltzmann constant. The initial conditions are given by

$$\begin{aligned} T(z, 0) &= 300 \\ n(z, 0) &= n_i, \end{aligned} \quad (3)$$

and the boundary conditions are as follows:

$$\begin{aligned} D \frac{\partial n}{\partial z} \Big|_{z=0} &= 0 \\ n(x \rightarrow \infty, t) &= n_i \\ -K_T \frac{\partial T}{\partial z} \Big|_{z=0} &= AI(t) - H(T - T_0) \\ T(z \rightarrow \infty, t) &= 300, \end{aligned} \quad (4)$$

where n_i is the intrinsic carrier concentration, K_T is the thermal conductivity, A is the absorption rate of the upper surface, and H is the heat transfer coefficient.

When the temperature is more than 3100 K, SiC produces gaseous silicon and solid/liquid graphite during laser irradiation. Different from stage 1, the decomposition and sublimation of SiC need to be considered in stage 2. Assuming that the sublimation rate, v , is constant, sublayer 1 and sublayer 2 are simplified to be composed of graphite only, and the semiconductor properties of SiC are ignored, the temperature change with time t and depth z in stage 2 can be expressed by

$$\frac{\partial T}{\partial t} = v \frac{\partial T}{\partial z} + \frac{\partial}{\partial z} \left(D_L \frac{\partial T}{\partial z} \right) + \frac{I(t)(1-R)\alpha e^{-\alpha z}}{C}. \quad (5)$$

Since stage 1 and stage 2 are in the same pulse, the initial conditions and boundary conditions are

set as

$$T_{\text{stage2}}(z, 0) = T_{\text{stage1}}(z, t_1), \quad (6)$$

$$-K_T \frac{\partial T}{\partial z} \Big|_{z=0} = (1-Q)A_1 I(t) + QA_2 I(t) - L_1 \rho_1 v_1 - L_2 \rho_2 v_2, \quad (7)$$

where t_1 is the moment when the temperature of the SiC substrate reaches 3100 K, L_1 , ρ_1 , and v_1 are, respectively, the decomposition enthalpy, density, and decomposition rate of SiC ($v_1 = 1354$ cm/s), L_2 , ρ_2 , and v_2 are the vaporization enthalpy, density, and evaporation rate of silicon ($v_2 = 195$ cm/s), and Q is the ratio of the laser energy directly acting on the SiC to the incident laser energy, and can be given by

$$Q = \frac{E}{E_0} = e^{-\alpha h}. \quad (8)$$

As h is assumed to be 50 nm, the calculated value of Q is 0.467. The parameters involved in the calculation are tabulated in Table I.

Numerical calculations by MATLAB are made according to the above equations and the temperature distribution of SiC for the first pulse is displayed in Fig. 7. Once the laser reaches the substrate, a large number of excess carriers ($\sim 10^{20}$ cm $^{-3}$) in SiC are generated. In the process of diffusion and recombination of photogenerated carriers, the substrate temperature rises rapidly through collision and coupling with the crystal lattice. In this process, Auger recombination plays a leading role, and surface recombination can be ignored [36,37]. It can be observed from Fig. 7(a) that the temperature reaches 3100 K after $t_1 = 3$ ns; the heating process goes from stage 1 to stage 2. As shown in Fig. 7(b), the computational surface reaches 4393 K, which is much higher than the boiling point of silicon (~ 2600 K) at the end of the laser irradiation. Therefore, the decomposed silicon will directly vaporize into the air and/or migrate to the edge of the irradiated area under the action of the temperature gradient, while the evaporation of graphite is negligible as the temperature is lower than the boiling point of graphite (~ 5100 K). On the other hand, at 291 nm away from the computational surface, the temperature is higher than 3100 K, which leads to the partial decomposition of SiC, due to the fact that SiC will melt violently when it reaches its melting point or above it. Therefore, in the calculation we assume that the distance between the location with a temperature of 3100 K and the surface at the end of the pulse should be consistent with the TDL at that number of pulses. Thus, it can be theoretically deduced that the thickness of the damaged layer is 291 nm at the end of the first pulse. After deducting the etching depth $d_1 = 42.5 \pm 3.6$ nm (test data), the theoretical value of the remaining damaged layer is about $d_2 = 248.5$ nm, which is almost consistent with our experimental result (255 ± 10 nm) [Fig. 3(e)].

After the first pulse, the phase near the surface is no longer SiC, but a mixture of silicon and graphite. Considering the low content of silicon in sublayer 1, and that the enthalpy of gasification of silicon is much smaller than that of graphite, the energy absorbed by silicon during the gasification process is negligible, and only the gasification of graphite and the decomposition of SiC are considered in the following calcu-

TABLE I. The parameters involved in the calculation.

Quantity	Value	Reference
D (cm ² /s)	$\frac{k_0 T}{q} \frac{6.825 \times 10^{12}}{1.05 \times 10^6 [\exp(\frac{1.92 \times 10^{-20}}{k_0 T}) - 1] + 6.5 \times 10^6 T^{1.5}} [(1 + \frac{135 \Delta n}{10^{18} T^{11.3 - (18/T)})}]^{2/3} - \frac{113}{T} (\frac{\Delta n}{10^{18}})^{1/3}$	[28]
E_g (J)	$5.26 \times 10^{-19} - 5.60 \times 10^{-23} \times \frac{T^2}{T+1100}$	[29]
R	0.27	[30]
α (cm ⁻¹)	1.4×10^5	[26]
γ (cm ⁶ /s)	$(7 \times 10^{-31} + \frac{3.5 \times 10^{-9}}{n \times T^{2/3}})(1 + \frac{n}{7.8 \times 10^{16} \times T})^{-2}$	[28]
D_L (cm ² /s)	$0.1895 + 8.07 \times e^{-T/144}$	[31]
K_T (W/cm·K)	$3.42 \times 10^3 \times T^{-1.256}$	[31]
C (J/K × cm ³)	$2.04 + 0.12 \times e^{-T/288}$	[31]
A_1	0.2	[32]
A_2	0.73	[30]
H (W/cm ² × K)	5	[30]
L_1 (kJ/g)	13.2	[33]
ρ_1 (g/cm ³)	3.24	
L_2 (kJ/g)	15	[34]
ρ_2 (g/cm ³)	2.3	
L_3 (kJ/g)	60	[34]
ρ_2 (g/cm ³)	1.87	
Q	0.467	
η	0.3	[35]

lation. Based on these assumptions, the endothermic term of thermal decomposition in Eq. (7) is corrected to

$$L\rho v = (L_2\rho_2 + L_3\rho_3)v_3, \quad (9)$$

where L_3 and ρ_3 are the vaporization enthalpy and density of graphite and $v_3 = 432$ cm/s is the evaporation rate, respectively. After the above corrections, the temperature distribution can be calculated and is shown in Fig. 8(a). Considering that the material in the region with temperature higher than 5103 K is vaporized, the etching depth is $d_1 = 160$ nm from theoretical analysis, which is larger than the experimental value of 108 nm. The reason for this discrepancy lies in the selection of Q value. From Eq. (8), the value of Q mainly depends on the thickness and the absorption coefficient of the graphite layer. Although the molar ratio of graphite is the highest in sublayer 1 and sublayer 2, there is still a small amount of silicon and SiC from XPS measurement. A correction factor, g , is introduced to describe the effect of mixture

phase rather than pure graphite phase on the value of Q . Obviously, the value of g is related to the thickness and absorption coefficient of different phases. As the absorption coefficient of silicon and SiC is greater than that of graphite for 248-nm laser, g is less than 1. After calculations, it is found that when $g = 0.96$, the calculation result is in good agreement with the experimental results, as shown in Fig. 8(b).

At the end of the 70th pulse, the temperature of the computational surface ($x = 0$) even reached 6000 K. At $x_1 = 120$ nm, $x_2 = 220$ nm, $x_3 = 360$ nm, and $x_4 = 480$ nm, the temperatures correspond to the boiling point of graphite (5103 K), the melting point of graphite (4500 K), the temperature at the interface of the damaged layer at the end of the 70th pulse, and the melting point of SiC (3100 K), respectively, as shown in Fig. 8(b). In the depth from $x = 0$ to $x_1 = 120$ nm, the temperature is higher than 5103 K; this area will be vaporized completely, i.e., the etched layer is $d_1 = 120$ nm. This value is almost the same as the etching depth of each pulse. In

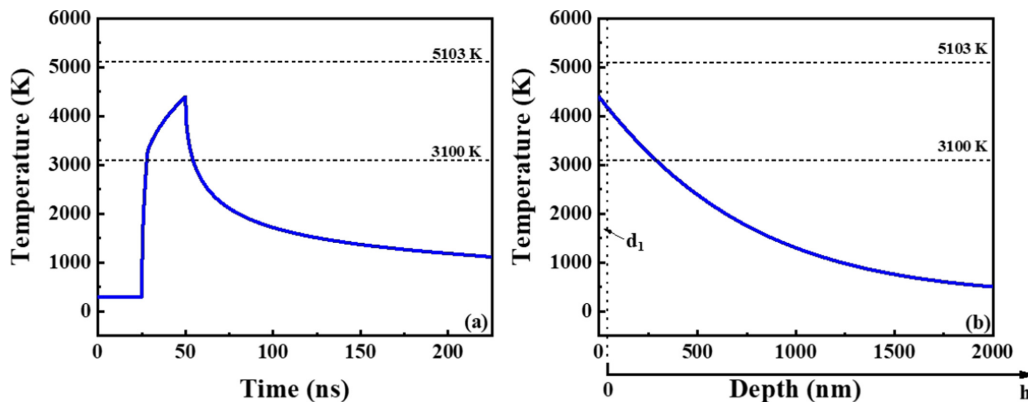


FIG. 7. (a) Relationship between the temperature of the SiC surface and the time for the first pulse. (b) Temperature distribution in the SiC body at the end of the first pulse.

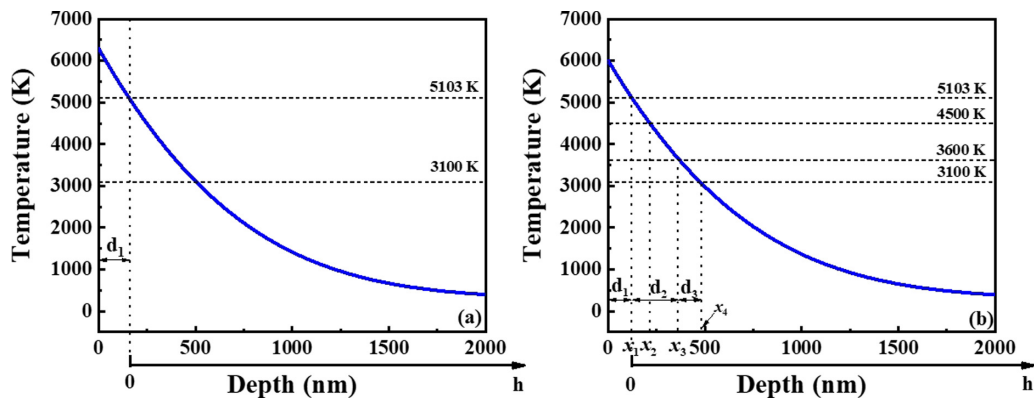


FIG. 8. (a) Temperature distribution of SiC during the 70th pulse irradiation. (b) At the end of the 70th pulse, the temperature distribution in the SiC body.

the depth from $x_1 = 120$ nm to $x_2 = 220$ nm, the temperature is in the range of 5103 ~ 4500 K, the graphite exists in the form of liquid, while the graphite is in the form of solid in the depth from $x_2 = 220$ nm to $x_3 = 360$ nm. It is not until $x_4 = 480$ nm that the temperature drops to 3100 K; the Si decomposed from SiC at this temperature is obviously in the gaseous phase. Because $x_2 = 220$ nm is the boundary between gas-phase and liquid-phase graphite, the gaseous Si generated in the depths of 220 ~ 480 nm is difficult to diffuse upward again when it reaches 220 nm because it is difficult for the gas to enter the liquid. Therefore, a large number of Si atoms are blocked in the region around 220 nm, and the percentage of Si in the region of 170–220 nm falls steeply from experimental results, forming the transition domain as discussed before. However, those Si atoms that were originally generated shallower than 220 nm evaporate very smoothly to the surface, thus creating such a trend of Si with depth as shown in Fig. 5(d3). The liquid graphite near the surface neither evaporates upward into the air nor diffuses downward into the solid graphite layer; they accumulate in the region of 120–170 nm.

It is notable that in Figs. 5(c6), 5(c12), and 5(d3), Si as well as graphite phases are still detected at $h = 500$ nm, mainly because SiC sublimates starting at 1600 K [38–40], but the sublimation rate is slow at this temperature and the pulse width of the laser is on the order of nanoseconds, so the damage is minor and cannot be directly observed from the SEM cross-sectional images. Yet when the temperature reaches the melting temperature of SiC (3100 K) [6], the decomposition reaction is intense and most of the SiC decomposes directly into gaseous Si and solid graphite, so the region with temperature higher than this value can be discerned directly in the SEM cross-sectional images due to the obvious melting traces. According to the calculation, the depth at which the temperature reaches 1600 K at the end of one pulse is $x = 864$ nm, which means that there is also a small part of SiC decomposition in the region of 480 nm $< x < 864$ nm, and the test area of Figs. 5(c6) and 5(c12) is $x = 620$ nm, which is just in this range, so that Si and graphite are detected.

As the region of $d_1 = 120$ nm has been vaporized, the thickness of the remaining theoretical damaged layer is $x_4 - x_1 = 360$ nm, which is smaller than the experimental value. The reason is that after the laser irradiation, part of the gaseous silicon and graphite will be recondensed and redeposited on

the surface during the cooling of the substrate, which is confirmed by XPS spectra and SEM surface image. In Fig. 3(b), it can be observed that the surface is covered with a layer of spherical nanoparticles with diameter of about 30–50 nm, which is approximately equal to the difference between theoretical and experimental values. More importantly, due to the effect of heat conduction, the region within the dashed line with the original undamaged thickness $d_3 = x_4 - x_3 = 120$ nm becomes a new damaged layer (Fig. 6). It can be obtained that the thickness of the damaged layer is the same at the end of each irradiation, that is, $d_1 = d_3$. This explains the phenomenon that the etching depth increases linearly with the number of pulses during the laser irradiation of SiC.

The effects of ArF (193 nm), KrF (248 nm), and XeCl (308 nm) nanosecond excimer laser ablation of SiC are analyzed according to our computational model, respectively. The reflectivity of SiC is 0.42 for a 193-nm wavelength laser and 0.27 for a 248-nm wavelength laser, so the substrate absorbs less energy at the same fluence irradiation for a 193-nm laser. In addition, due to high absorption coefficient of the 193-nm laser by graphite, most of the laser energy is absorbed in the region near the surface, and the energy that penetrates the graphite layer and acts directly on the SiC is reduced, so the temperature rise becomes lower, leading to a lower ablation rate, which is consistent with the experimental phenomenon. Although the 308-nm laser has the advantage of low reflectivity, it is offset by its very small absorption coefficient to SiC compared to the 248-nm laser; the temperature rise is still minor, resulting in a lower ablation rate. This is why KrF excimer laser is most widely used in laser ablation of SiC.

The model of laser ablation of SiC has been reported previously, but there are some shortcomings. For example, Bet *et al.* treated the physical parameters as constants in their calculation [41]. In fact, the main thermal parameters of SiC are temperature dependent. Treating them as constants would result in a lower temperature distribution according to our calculations. Gupta *et al.* did not consider the decomposition and evaporation of SiC at high temperatures [42]. However, neglecting these factors will lead to a larger temperature distribution since the evaporation of the substances absorbs part of the laser energy. Mohammed *et al.* did not consider the composition of the substance and their corresponding ratios in their calculations despite the fact that the decomposition

of SiC was taken into account [16]. The different absorption coefficients of Si and graphite for the laser and the variation in their thermal properties lead to a bias in their calculations compared to our work. Our calculation model takes the temperature dependence of the thermal parameters of SiC, the decomposition of SiC at high temperatures with the evaporation of the substance, and the change of the substance phase into account. More importantly, the calculation model is reasonably established based on the experimental results which make our calculation results follow the experimental phenomena well.

Nevertheless, our model still has many shortcomings. On the one hand, only the temperature-driven processes are considered, and the dynamics-driven processes are ignored; on the other hand, any quantitative evaluation of the redeposited material is also overlooked. Third, the plasma-shielding phenomenon is not taken into account. As the length of the laser pulse width used in the experiments is of the order of nanoseconds, when the pulse goes on, the temperature and enthalpy of the vapor above SiC substrate continues to increase, thus absorbing more laser energy to form dense plasma. The plasma then absorbs the incident laser energy (dominated by inverse bremsstrahlung absorption), thus acting as a plasma shielding, so that the energy delivered to SiC substrate is correspondingly reduced. In our experiment we used a laser energy of $4.5 \pm 0.1 \text{ J/cm}^2$ and the material present above the surface should be only gaseous silicon or gaseous graphite; both of them form a plasma that absorbs less than 5% of the laser energy under such condition [43]. Hence for our model, plasma shielding will reduce the temperature of the substrate to some extent. Neglecting its effect would lead to a bias in our calculated etched layer thickness d_1 compared to the experimental value. This is the reason why the two are deviated.

IV. CONCLUSION

Modeling of KrF excimer laser ablation of SiC was investigated. The relationship between the etching depth and the number of pulses is linear. The uniform damaged layer is observed by SEM cross-sectional morphology and its thickness in constant unit pulse number is more than 10. Si and graphite generate when the laser irradiates on the SiC surface, which is verified by XPS. *In situ* XPS analysis demonstrates that the damaged layer can be roughly considered as two mixture layers and a graphite layer located in between, independently of the pulse number, thereby establishing a calculated model. The temperature distribution inside the SiC during laser irradiation is numerically calculated by reasonable assumptions and approximations. The result shows that the equilibrium between the thickness of evaporation and the thickness of the newly formed damaged layer is essentially due to the uniform temperature distribution generated by each pulse, so that the uniform damaged layer is formed and the etching rate is fixed. The research on the decomposition of SiC after laser irradiation, the distribution of material within the damaged layer, and the mechanism of laser etching of SiC has a significant reference for laser etching, laser drilling, laser doping, and other techniques in MEMS device manufacturing process. Next, we will try to apply the laser-processing technology based on the laser ablation SiC mechanism to the fabrication of photoconductive switches.

ACKNOWLEDGMENT

This work was supported by the Joint Fund of the National Natural Science Foundation of China (NSFC) and the China Academy of Physics (NASF) under Grant No. U183014.

-
- [1] W. F. Koehl, B. B. Buckley, F. J. Heremans, G. Calusine, and D. D. Awschalom, *Nature (London)* **479**, 85 (2011).
 - [2] I. P. Nikitina, K. V. Vassilevski, N. G. Wright, A. B. Horsfall, A. G. O'Neill, and C. M. Johnson, *J. Appl. Phys.* **97**, 083709 (2005).
 - [3] Z. T. Wang, W. Liu, and C. Q. Wang, *J. Electron. Mater.* **45**, 267 (2016).
 - [4] Y. Hishida, M. Watanabe, K. Nakashima, and O. Eryu, *Mater. Sci. Forum* **338–342**, 873 (2000).
 - [5] S. Ahmed, C. J. Barbero, and T. W. Sigmon, *Appl. Phys. Lett.* **66**, 712 (1995).
 - [6] A. N. Samant, C. Daniel, R. H. Chand, C. A. Blue, and N. B. Dahotre, *Int. J. Adv. Manuf. Technol.* **45**, 704 (2009).
 - [7] A. Ikeda, D. Marui, R. Sumina, H. Ikenoue, and T. Asano, *Mater. Sci. Semicond. Proc.* **70**, 193 (2017).
 - [8] J. Zhang, K. Sugioka, S. Wada, H. Tashiro, and K. Toyoda, *Appl. Phys. A* **64**, 367 (1997).
 - [9] B. Pecholt, M. Vendan, Y. Dong, and P. Molian, *Int. J. Adv. Manuf. Technol.* **39**, 239 (2008).
 - [10] W. Robin, *Acc. Chem. Res.* **14**, 246 (1981).
 - [11] Y. Hibi, Y. Enomoto, K. Kikuchi, N. Shikata, and H. Ogiso, *Appl. Phys. Lett.* **66**, 817 (1995).
 - [12] J. R. Meyer, F. J. Bartoli, and M. R. Kruer, *Phys. Rev. B* **21**, 1559 (1980).
 - [13] K. Zekentes, I. Zergioti, A. Klini, and G. Constantinidis, *Mater. Sci. Forum* **527–529**, 1119 (2006).
 - [14] C. Dutto, E. Fogarassy, and D. Mathiot, *Appl. Surf. Sci.* **184**, 362 (2001).
 - [15] R. Reitano and P. Baeri, *Nucl. Instrum. Methods* **116**, 369 (1996).
 - [16] A. F. Mohammed, Q. A. Al-Jarwany, A. J. Clarke, T. M. Amaral, J. Lawrence, N. Kemp, and C. D. Walton, *Chem. Phys. Lett.* **713**, 194 (2018).
 - [17] M. Birnbaum, *J. Appl. Phys.* **36**, 3688 (1965).
 - [18] J. F. Young, J. E. Sipe, J. S. Preston, and H. M. van Driel, *Appl. Phys. Lett.* **41**, 261 (1982).
 - [19] J. Bonse, J. Krüger, and A. Rosenfeld, *J. Appl. Phys.* **106**, 104910 (2009).
 - [20] J. Bonse and J. Krüger, *J. Appl. Phys.* **108**, 034903 (2010).
 - [21] M. Huang, F. Zhao, Y. Cheng, N. Xu, and Z. Xu, *ACS Nano* **3**, 4062 (2009).
 - [22] G. Miyaji and K. Miyazaki, *Opt. Express* **16**, 16265 (2008).
 - [23] G. D. Tsibidis, C. Fotakis, and E. Stratakis, *Phys. Rev. B* **92**, 041405(R) (2015).

- [24] K. L. Smith and K. M. Black, *J. Vac. Sci. Technol. A* **2**, 744 (1984).
- [25] F. P. Bundy, *Physica A* **156**, 169 (1989).
- [26] Y. Cheng, W. Y. Lu, T. Wang, and Z. Z. Chen, *J. Appl. Phys.* **119**, 225705 (2016).
- [27] M. I. Gallant and H. M. van Driel, *Phys. Rev. B* **26**, 2133 (1982).
- [28] S. Patrik and K. Jarasiūnas, *J. Phys. D: Appl. Phys.* **46**, 265304 (2013).
- [29] A. Galeckas, P. Grivickas, V. Grivickas, V. Bikbajevs, and J. Linnros, *Phys. Status Solidi A* **191**, 613 (2002).
- [30] Z. Tian, N. R. Quick, and A. Kar, *Acta. Mater.* **54**, 4273 (2006).
- [31] R. Wei, S. Song, K. Yang, Y. Cui, and Y. Peng, *J. Appl. Phys.* **113**, 053503 (2013).
- [32] M. Hanfland, K. Syassen, and R. Sonnenschein, *Phys. Rev. B* **40**, 1951 (1989).
- [33] J. Chen, G. U. Lin, W. Zhao, and M. Guagliano, *Chin. J. Aeronaut.* **34**, 37 (2021).
- [34] D. Bäuerle, *Laser Processing and Chemistry* (Springer, Berlin, 2011).
- [35] T. V. Blank, Y. A. Gol'dberg, E. V. Kalinina, O. V. Konstantinov, A. O. Konstantinov, and A. Hallen, *Tech. Phys. Lett.* **27**, 776 (2001).
- [36] E. J. Yoffa, *Phys. Rev. B* **21**, 2415 (1980).
- [37] E. J. Yoffa, *Appl. Phys. Lett.* **36**, 37 (1980).
- [38] W. H. Soe, K. H. Rieder, A. M. Shikin, V. Mozhaikii, A. Varykhalov, and O. Rader, *Phys. Rev. B* **70**, 115421 (2004).
- [39] S. Adachi, M. Mohri, and T. Yamashina, *Surf. Sci.* **161**, 479 (1985).
- [40] L. Muehlhoff, W. J. Choyke, M. J. Bozack, and J. T. Yates, *J. Appl. Phys.* **60**, 2842 (1986).
- [41] S. Bet, N. Quick, and A. Kar, *Acta. Mater.* **55**, 6816 (2007).
- [42] S. Gupta, B. Pecholt, and P. Molian, *J. Mater. Sci.* **46**, 196 (2011).
- [43] N. M. Bulgakova, A. V. Bulgakov, and L. P. Babich, *Appl. Phys. A* **79**, 1323 (2004).